Mechanical Systems and Signal Processing 174 (2022) 109093

Contents lists available at ScienceDirect

Mechanical Systems and Signal Processing

journal homepage: www.elsevier.com/locate/ymssp

Non-contact vehicle weighing method based on tire-road contact model and computer vision techniques

Xuan Kong [a], Jie Zhang [b], Tengyi Wang [b], Lu Deng [c,*], C.S. Cai [d,e]

[a] Key Laboratory for Damage Diagnosis of Engineering Structures of Hunan Province, College of Civil Engineering, Hunan University, Changsha 410082, China
[b] College of Civil Engineering, Hunan University, Changsha 410082, China
[c] Key Laboratory for Damage Diagnosis of Engineering Structures of Hunan Province, College of Civil Engineering, Hunan University, Changsha 410082, China
[d] Dept. of Bridge Engineering, School of Transportation, Southeast Univ., Nanjing 211189, Jiangsu, China
[e] Dept. of Civil and Environmental Engineering, Louisiana State Univ., Baton Rouge, LA 70803, United States

ARTICLE INFO

Communicated by Javad Baqersad

Keywords:
Vehicle weigh-in-motion
Computer vision
Tire-road contact
Image segmentation
Character recognition

ABSTRACT

Vehicle overloading is a very common phenomenon. The overloaded vehicles not only cause severe damage to the road/bridge and shorten its service life, but also likely lead to traffic accidents. Therefore, the identification of vehicle load is of great importance to the management of overload vehicles and can also provide valuable information for the design and maintenance of transportation infrastructures. The commonly used vehicle weighing methods including static weighing, pavement weigh-in-motion (PWIM), and bridge weigh-in-motion (BWIM) are contact technologies with weakness such as cumbersome installation, poor durability, short service life, and high maintenance cost. It is desirable to have a non-contact vehicle weight identification method without any sensor or scales on/under the road and bridge. Thus, the present study proposed a non-contact method based on the tire-road contact model and computer vision techniques. Firstly, the tire-road contact model is theoretically derived based on the Hertz contact theory, and the relationship between the tire vertical force and the tire deformation is obtained. Then, computer vision techniques such as the image segmentation and character recognition are adopted for the identification of the tire deformation and inflation pressure that are combined with the theoretical model to determine the tire vertical force and then the vehicle weight. Finally, the field test on passenger cars and trucks are conducted to verify the proposed method. The results indicate that the proposed method has a better performance than those methods in the literature, and shows a high accuracy and robust performance in vehicle weight identification under different conditions of inflation pressure, vehicle weight, motion state, and tire type.

1. Introduction

With the rapid growth of highway transportation industry in recent years, the phenomenon of vehicle overloading has become very common, especially in China. The overloaded vehicles not only cause severe damage to the road/bridge and shorten its service life, but

* Corresponding author.
E-mail addresses: kongxuan@hnu.edu.cn (X. Kong), zhangjietm@hnu.edu.cn (J. Zhang), wangty96@hnu.edu.cn (T. Wang), denglu@hnu.edu.cn (L. Deng), cscai@seu.edu.cn, cscai@lsu.edu (C.S. Cai).

https://doi.org/10.1016/j.ymssp.2022.109093
Received 26 October 2021; Received in revised form 22 March 2022; Accepted 24 March 2022
Available online 12 April 2022

also likely lead to traffic accidents. On one hand, when a vehicle is over the weight limit, it increases the risk of bridge collapse and road failure since the bridges/roads are designed to sustain a limited weight and stress. The constant heavy weight on the roads/bridges also leads to a higher rate of repair. On the other hand, all trucks have weight limits that are safe for drivers to maneuver, that is, an overweight will make the drivers difficult to control and brake the vehicle, increasing the possibility of accidents. Therefore, the identification of vehicle load is of great importance to the management of overloaded vehicles and provides valuable information for the design and maintenance of transportation infrastructures [1–3].

The commonly used vehicle weighing methods include static weighing, pavement weigh-in-motion (PWIM), and bridge weigh-in-motion (BWIM). The static weighing as a traditional method utilizes a static electronic weighing scale to obtain the vehicle weight. The static weighing technology is widely used for weight restriction and overload enforcement in the United States and European countries due to its high accuracy [4,5]. However, the static weighing method requires the vehicle to completely stop, which has a very low efficiency and could easily cause traffic congestion. In addition, it has the disadvantages of cumbersome installation, poor durability, and immovability [6]. Weigh-in-motion (WIM) is a method to capture the axle and gross weights as the vehicles drive over the sensors at a normal or reduced speed without stopping, which makes it more efficient than the static weighing method. The WIM system installed on the pavement is referred as the PWIM. Different types of sensors are used for the PWIM measurement, including the bending plate, single load cell, strip sensors such as the piezoelectric and piezo-quartz sensors [7]. Despite the PWIM has a better efficiency, it is generally less accurate than the static electronic weighing scale because the PWIM measurement is sensitive to the number of sensors, road roughness, and ambient temperature. Those factors have a significant impact on the quality and reliability of the measured data. Gajda et al. [8] studied the reasonable number of sensors required by the PWIM to ensure the accuracy of vehicle weight measurement. Liu et al. [9] analyzed the effects of road geometry, roughness, and slope to the PWIM systems. Among them, the road roughness shows the greatest impact on the measurement accuracy of PWIM. Burnos and Rys [10] through field tests indicated that the vehicle speed and ambient temperature were the critical factors affecting the accuracy of PWIM. Moreover, the durability of the sensors and PWIM system itself is a big issue. During the installation and operation, the pavement needs to be excavated, and the sensors embedded in the pavement are vulnerable under the constant rolling of passing vehicles, leading to short service life and high maintenance cost.

Another type of WIM system is the bridge weigh-in-motion (BWIM), using an instrumented bridge as the weighing platform. The BWIM is an indirect method by measuring the bridge dynamic response such as the bridge strain or displacement to identify the weight of vehicles traveling on the bridge [11]. Moses [12] proposed the BWIM method in 1979 and established the basic framework of BWIM based on the relationship between the moment influence lines of the bridge and the positions of vehicle loads. Richardson et al. [13] reviewed the development of vehicle weighing method from static weighing to BWIM and compared the accuracy of several BWIM devices. Yu et al. [14] presented a comprehensive review of BWIM method and its applications. Cardini and Dewolf [15] adopted the strain-area method into BWIM and realized the long-term monitoring of a simply supported bridge on an interstate highway, but the BWIM could only obtain the gross vehicle weight. Ojio et al. [16] proposed a reaction force method to identify the axle load of vehicles, but the measurement of the support force is difficult in practical applications, and this method is not suitable for the long-term traffic load monitoring. Recently, He et al. [17,18] proposed a virtual simply-supported beam method that could be used to eliminate the influence of boundary condition and improve the accuracy of vehicle weight identification based on the combination of the virtual axle method and Moses's algorithm. The BWIM method has advantages of good sensor durability, high identification accuracy, and convenient installation. However, the BWIM is susceptible to the environment factors (e.g., vibration and noise), since the vehicle-induced bridge vibration is very complex. Meanwhile, BWIM still requires installation of a sensor system on bridges, which could be costly. Hence, it is necessarily to develop a cost effective and robust vehicle weighing method with high accuracy for the practical application.

The computer vision (CV) technology with advantages such as simple installation, low cost, and contactless measuring has been developed rapidly in recent years, and has been widely applied in measuring the structural displacement, strain, and modal information. A few researchers have combined CV with PWIM to obtain the spatio-temporal distribution of vehicle loads. Chen et al. [19] combined the PWIM weight data and the camera information to identify the spatio-temporal distribution of vehicle loads on the long-span Hangzhou Bay bridge. Dan et al. [20] put forwarded the fusion of PWIM system and CV system, in which the vehicle weight was obtained through the PWIM before entering the bridge and the vehicle trajectory on the bridge was tracked through multiple cameras. Ge et al. [21] proposed an improved method based on YOLO-V3 convolutional neural network (CNN) for the traffic load monitoring. In addition, some scholars measured the bridge dynamic response through CV and combined it with BWIM method to identify the weight of vehicles traveling on the bridge. Ojio and Lydon et al. [22,23] proposed contactless BWIM method using two cameras, one camera to measure the bridge deflection and the other camera to determine axle spacing. Jian et al. [24] and Xia et al. [25] proposed a traffic sensing method that combined the deep learning-based CV with the influence line theory to automatically identify vehicle parameters such as the weight, speed, type, and axles of passing vehicles on short and medium span bridges. Dong et al. [26] used portable cameras to monitor the bridge deflection induced by moving vehicles, and estimate the vehicle load distribution using the influence line of the lateral live load distribution factors. According to the above literature review, most of the existing CV-based vehicle identification methods acquire the vehicle weight through the weighing scale, sensors, or bridges. It is desirable to have a non-contact vehicle weight identification method without any sensors or scales on/under the road and bridge. One alternative is to identify the tire-road contact forces based on the tire deformation using CV techniques. Currently, only Feng et al. [27,28] have conducted some preliminary study, in which the tire-road contact force is obtained by multiplying the inflation pressure with the contact area measured by CV. However, their method assumes that the tire inflation pressure is equal to the contact pressure, which is unreasonable for many cases, especially for truck tires. In addition, Anoop et al. [29] proposed a vibration signals-based method to measure tire deformation and pressure through sensors installed at the wheel center. Although this method has advantages of easy to deploy, low cost, and high accuracy, it is

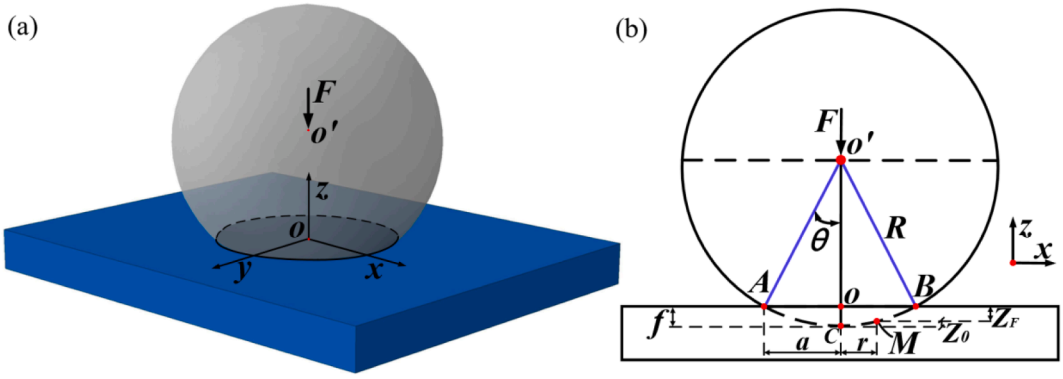

Fig. 1. Sphere-plane contact model: (a) three-dimensional diagram; (b) cross section.

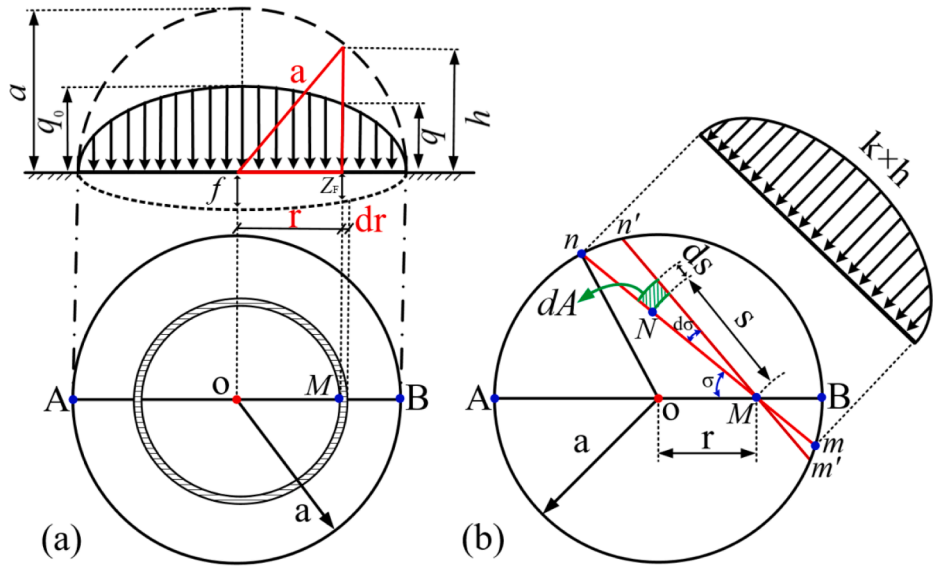

Fig. 2. Relationship between tire deformation and contact pressure: (a) pressure distribution; (b) deflection point and pressure point.

still a contact method that requires installing sensors on each tire of the vehicle and only the weight of the installed vehicle can be measured.

The objective of this study is to propose a non-contact vehicle weight identification method based on the tire-road contact theoretical model and computer vision technology. The tire-road contact model is theoretically derived based on the Hertz contact theory. Computer vison techniques such as the image segmentation and character recognition are adopted for the identification of the tire deformation and pressure, which are used to determine the tire vertical force and then the vehicle weight. The field test of passenger cars and trucks are conducted to verify the proposed method.

2. Theoretical model of Tire-road contact

The tire-road contact is a very complex issue. In the present study, the theoretical model of tire-road contact is established by improving the Hertz contact theory [30]. The contact between the tire and the road can be simplified as a contact between an elastic sphere and a rigid half-space, that is, sphere-plane contact. The contact model is schematically shown in Fig. 1, R is the tire radius, point A and B are the edge points of the contact area, a is half of the tire-road contact length, θ is the radius angle of the contact half length, and F is the vertical force applied on the tire center. The detailed theoretical derivations of the three primary equations (i.e., geometric equation, equilibrium equation, and physical equation) are described below.

2.1. Geometrical equation

For the arbitrary point M on the contact area, it has the following deformation condition as,

$$f = Z_0 + Z_F \Rightarrow Z_F = f - \frac{r^2}{2R} \tag{1}$$

where f is the vertical movement of the tire center, equal to the vertical deflection of the tire bottom, i.e., the vertical distance between point C and point B, Z_0 is the original height of point M to the road surface, Z_F is the vertical distance between point M and point B, and r is the horizontal distance from point M to point C. It is noteworthy that the contact pressure at point M exists only after the point contacts with the road, that is, the pressure of point M mainly depends on the deflectionZ_F.

2.2. Equilibrium equation

As shown in Fig. 2(a), the pressure distribution of the contact area is assumed to follow the hemispherical distribution. That is, the contact pressure q at any point on the contact area is proportional to its hemispherical height as,

$$q = kh \tag{2}$$

where k is the proportional constant. Since a linear elastic material is assumed, the pressure distribution on the contact area is the same as the strain distribution. Thus, the maximum pressure is at the central point of the contact area, i.e., point O. In terms of Eq. (2) we have the maximum pressure as, $q_0 = ka$. Thus, we can determinate the value of the proportional constant, i.e., $k = q_0/a$.

Based on the force equilibrium, the sum of the pressure on the contact area is equal to the vertical force as,

$$F = \int_0^a 2\pi r dr \cdot q = \int_0^a 2\pi r dr \cdot \frac{q_0}{a} \cdot \sqrt{a^2 - r^2} = \frac{2\pi a^2 q_0}{3} \tag{3}$$

2.3. Physical equation

In the tire-road contact problem, the vehicle load F applied on the tire axle is eventually transmitted as the contact pressure on the contact area, resulting in the tire deformation. The vertical deflection dZ_F at the arbitrary point M caused by the contact pressure at any point N on the contact area can be obtained using the Boussinesq's equation as [31],

$$dZ_F = \frac{1 - \lambda_t^2}{\pi E_t} \frac{dF}{s} \tag{4}$$

where λ_t is the Poisson's ratio of tire, E_t is the elastic modulus of tire, and s is the distance between the deflection point M and the pressure point N. By applying the integration on the entire contact area, we can obtain the vertical deflection at point M due to the contact pressure of the entire contact area,

$$Z_F = \frac{1 - \lambda_t^2}{\pi E_t} \iint \frac{dF}{s} = \frac{1 - \lambda_t^2}{\pi E_t} \iint \frac{qdA}{s} \tag{5}$$

As shown in Fig. 2(b), the secant line mn passes points M and N, with the angle σ from the line AB. The angle between the secant line mn and the other secant line $m'n'$ is $d\sigma$. The radius of the two arcs are s and $s + ds$. Thus, the differential pressure at point N can be expressed as, $dF = qdA = qsdsd\sigma$. Eq. (5) can be simplified as,

$$Z_F = \frac{1 - \lambda_t^2}{\pi E_t} \iint \frac{qdA}{s} = \frac{1 - \lambda_t^2}{\pi E_t} \int d\sigma \int qds = \frac{1}{\pi E_e} \int d\sigma \int qds \tag{6}$$

where E_e is the equivalent elastic modulus of the tire-road at the contact area as,

$$E_e = E_t / \left(1 - \lambda_t^2\right) \tag{7}$$

For the determination of the equivalent elastic modulus, the readers are referred to the detailed derivation in Appendix A.

According to Eq. (2), we have,

$$\int qds = \int kh\, ds = \frac{q_0}{a} A \tag{8}$$

where $A = \pi\left(a^2 - r^2 sin^2\sigma\right)/2$ is the semicircle area with the diameter of secant line mn. By substituting Eq. (8) into Eq. (6), we have,

$$Z_F = \frac{1}{\pi E_e} \iint qdsd\sigma = \frac{1}{\pi E_e} \times \frac{q_0 \pi}{2a} \int \left(a^2 - r^2 sin^2\sigma\right) d\sigma = \frac{q_0}{4aE_e} (2a^2 - r^2) \tag{9}$$

By combining Eqs. (1), (3), and (9), the vertical deflection f and the half contact length a are calculated as:

$$f = \sqrt[3]{\frac{9}{16R} \left(\frac{1}{E_e}\right) F^2} \tag{10}$$

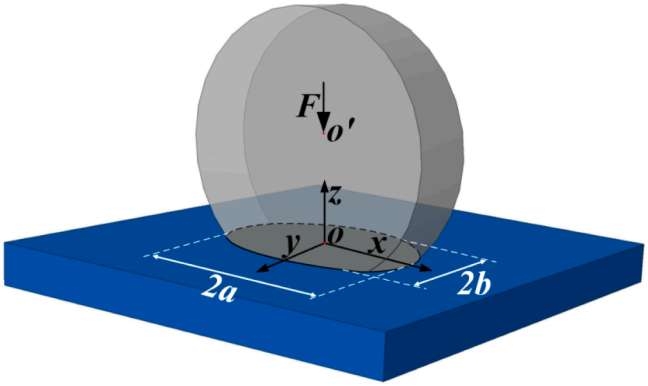

Fig. 3. Cylinder-plan contact model.

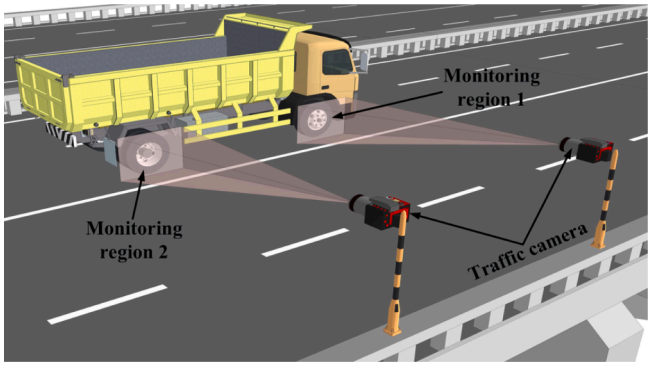

Fig. 4. System configuration of CV-based vehicle weighing method.

$$a = \sqrt[3]{\frac{3R}{4}\left(\frac{1}{E_e}\right)F} \tag{11}$$

Eqs. (10) and (11) establish the relationship between the tire deformation and the vertical load. In the above sphere-plane model shown in Fig. 1, the tire model is isotropic, which assumes that the tire-road contact has the same distribution in the length and width directions. However, based on the tire configuration, the width direction is totally different from the length direction. Compared to the sphere-plane model, the cylinder-plane model is more suitable for the tire-road contact [32]. Fig. 3 presents the cylinder-plane contact model, in which b is half of the tire-road contact width.

In the cylinder-plane model, the elliptical distribution is assumed for the pressure distribution on the contact area as,

$$\overline{q}(x,y) = \frac{3F}{2\pi ab}\sqrt{1-\left(\frac{x}{a}\right)^2-\left(\frac{y}{b}\right)^2} \tag{12}$$

According to the above derivation procedure, the vertical deflection f and the half contact length a can be obtained as,

$$f = \frac{F}{\pi E_e b}\times\left[1-ln\left(\frac{FR}{\pi E_e b^3}\right)\right] \tag{13}$$

$$a = \sqrt{\frac{4RF}{\pi E_e b}} \tag{14}$$

The equivalent elastic modulus can be calculated by tire deformation and pressure as detailed in Appendix A. Eqs. (13) and (14) can be rewritten as,

$$F = \frac{\pi E_e b f}{1+ln\left(\pi E_e b^3\right)-ln(FR)} \tag{15}$$

$$F = \frac{\pi E_e b a^2}{4R} \tag{16}$$

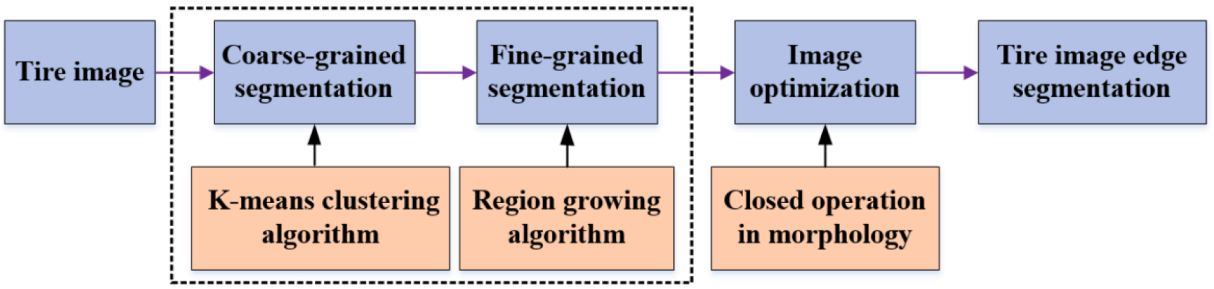

Fig. 5. Segmentation algorithm of tire image.

Fig. 6. Coarse segmentation using clustering algorithm: (a) original tire image; (b) rim edge segmentation; (c) tire edge segmentation.

Eqs. (15) and (16) establish the relationship between the tire load, tire vertical deflection, and inflation pressure. Thus, once the tire deformation and inflation pressure are known, the vertical load on the tire can be calculated.

3. Methodology of computer Vision-based vehicle weighing

A computer vision-based weight identification method is proposed for vehicles. Fig. 4 shows the system configuration of the proposed method. Visual-image acquisition devices such as traffic cameras are placed on the roadside to capture the tire images. Computer vision techniques such as the image segmentation and character recognition are then applied to obtain the tire deformation and pressure, and the vehicle weight can be identified according to the theoretical formulas derived above. The following sections will give a detailed introduction on the methodology including the image segmentation, the character recognition, and the general procedure.

3.1. Image segmentation

An automatic edge segmentation algorithm was proposed to extract the edges of the tire and rim. The algorithm includes image coarse/fine grained segmentation and image optimization, as presented in Fig. 5. To detect the tire edge from the image background, the K-Means clustering algorithm was used for coarse segmentation, the region growing algorithm was used subsequently for fine segmentation, and the closed operation in morphology was used finally for eliminating the edge noise.

Firstly, the coarse-grained segmentation using K-Means clustering algorithm [33,34] was applied to achieve the clustering of tire and rim regions. The procedure of the K-Means clustering algorithm is as follows:

The number of the 3 clusters (tire, rim, background) and the 3 initial cluster centers μ_i ($1 < i$ less than 3) are randomly selected from the images.

The cluster similarity is estimated using the Euclidean distance. The Euclidean distance from the pixel z_{ij} ($1 < j < Q_i$) in the i groups to the cluster center μ_i is calculated as follow:

$$d(z_j, \mu_i) = \sqrt{\sum_{j=1}^{Q_i} (z_{ij} - \mu_i)^2} \tag{17}$$

where Q_i is the set of pixels in the i groups; μ_i is the cluster center in the i groups; and z_{ij} is the j-th pixel in the i groups.

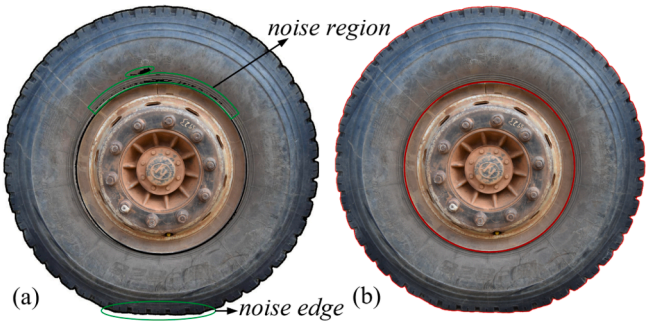

Fig. 7. Tire image segmentation: (a) detected edge using coarse/fine grained algorithm; (b) final edge after morphological operation.

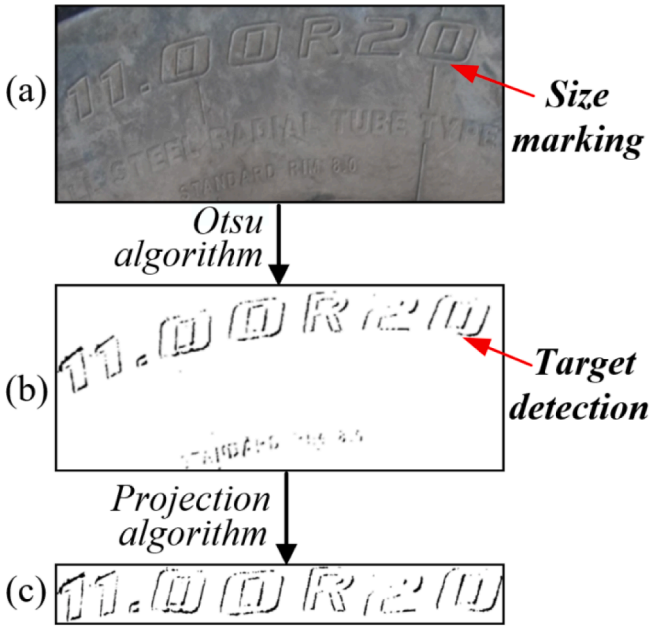

Fig. 8. Character detection and positioning: (a) original size marking; (b) detection of size marking; (c) position of size marking.

The Euclidean distances of the 3 clusters are added together, and the sum J of each group is calculated in the image pixels based on the following equation:

$$J = \sum_{i=1}^{3} \sum_{j=1}^{Q_i} \left(z_{ij} - \mu_i\right)^2 \tag{18}$$

According to the similarity between the pixels and cluster center by Euclidean distance, the position of the cluster center is updated. To understand the update process of sum J, white-box model is provided to explain the correctness and wrongness of the clusters, and the segmentation results are explicable [35,36]. The clustering procedure stops until the J no longer decreases or all pixels of the image are calculated.

With respect to the original tire image shown in Fig. 6(a), the three clusters were selected, i.e., background, rim, and tire. The coarse edges of the rim and tire were segmented by the K-Means clustering algorithm, as shown in Fig. 6(b) and (c).

Subsequently, the region growing segmentation algorithm (RGSA) was applied for fine segmentation. The RGSA is based on the aggregation of pixels with similar properties such as color, gray, texture features, etc. [37]. The RGSA consists of three main components: initial seed determination, region growing criterion, and region stopping condition. The tire edges extracted using the K-Means clustering and the RGSA were shown in Fig. 7(a). It shows that the edges of tire can be clearly obtained using coarse/fine grained segmentation. Nevertheless, the obtained tire edges are not smooth with some noises.

In order to eliminate the edge noise, the morphological closing operations including the dilation and erosion operations are applied to optimize the edge [38]. Dilation operation was used to expand the tire edge, and the missing pixels were filled up to obtain

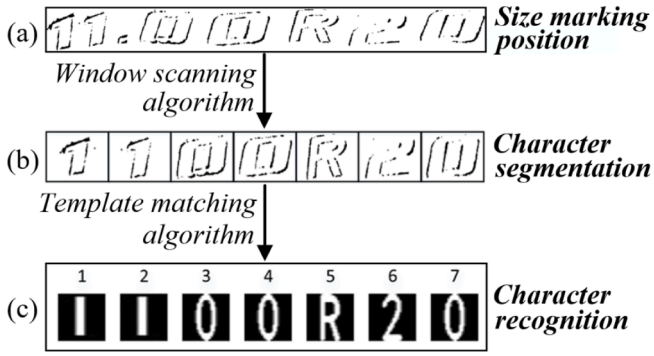

Fig. 9. Character segmentation and recognition: (a) position of size marking; (b) segmentation of character; (c) recognition of character.

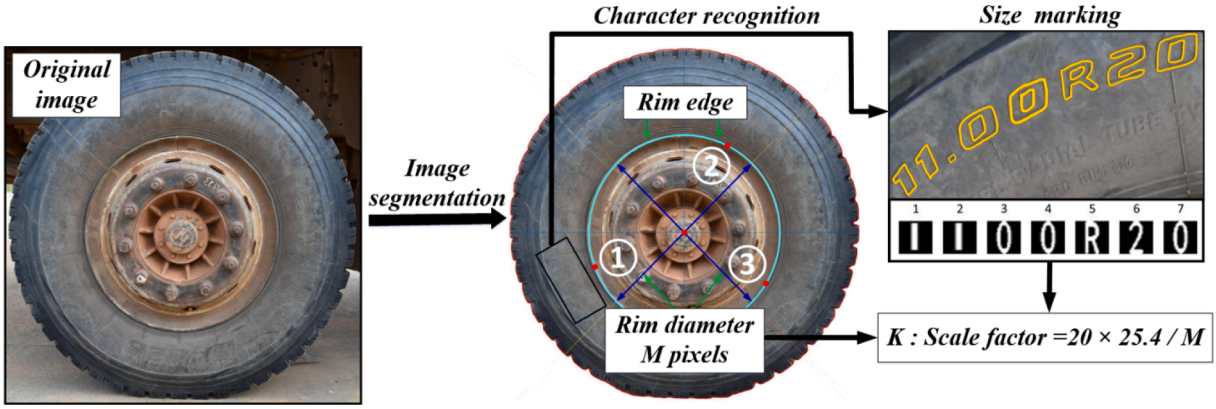

Fig. 10. Scale factor of the image.

continuous tire edges. The erosion operation removed the noisy pixels between the tire edge and background. Finally, a smooth, continuous, and complete tire edge were obtained, as shown in Fig. 7(b).

3.2. Character recognition

The tire sidewall contains some useful information such as the tire brand, tread pattern, size marking, inflation pressure, load index, and speed symbol or rating, etc. Among them, the size marking and inflation pressure on the tire sidewall are essential parameters for the vehicle weight identification. Herein, the character recognition technique was adopted as detailed below.

3.2.1. Character detection and positioning

The color between the characters and the tire is very close as shown in Fig. 8(a), which makes it difficult to detect the characters from the sidewall image. Herein, the Otsu algorithm [39] and projection algorithm [40] were adopted for the character detection and positioning in the tire sidewall image.

The Otsu algorithm is a very useful thresholding method to separate the foreground pixels from the background, which is a variance-based technique searching for the threshold minimizing the within-class variance between the foreground and background pixels. By applying the Otsu algorithm, the character zone can be detected from the sidewall image as shown in Fig. 8(b). However, there are still some unrelated objects detected. In order to accurately detect the characters, the image projection algorithm was applied to obtain the accurate position of the characters. First, the coordinate transformation method was used to convert the arc marking into the rectangular image. Specifically, the geometric transformation of polar coordinates and rectangular coordinates is used to definite the corresponding relationship between “arc graph” and “rectangular graph”. The polar_trans_image_Ext operator transforms the arc graph of tire marking into a rectangular graph. After applying the projection algorithm, the size marking was accurately located as shown in Fig. 8(c). The recognition process of this projection algorithm is affected by scaling, blur, and rotations. The robustness of these parameters is well analyzed based on the integral projection algorithm [41,42].

3.2.2. Character segmentation and recognition

After the region of the character was positioned, the window scanning algorithm was used for the character segmentation and recognition [43]. The window scanning algorithm divides the characters in the way of row and column scanning. That is, the upper and

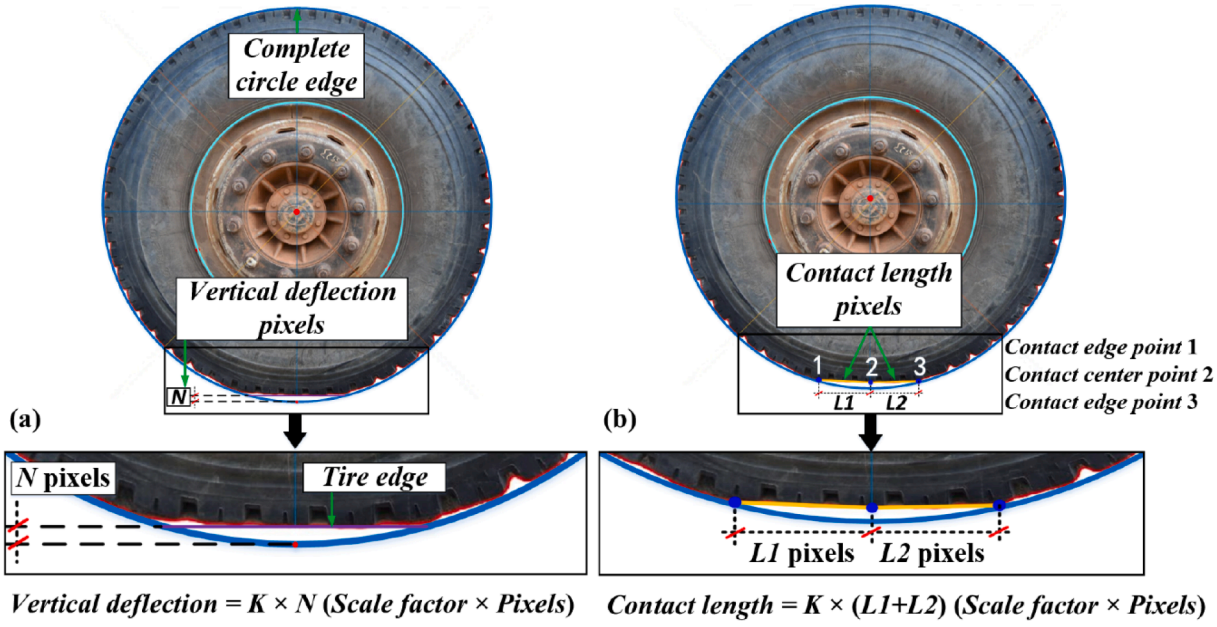

Fig. 11. Identification of tire deformation: (a) vertical deflection; (b) contact length.

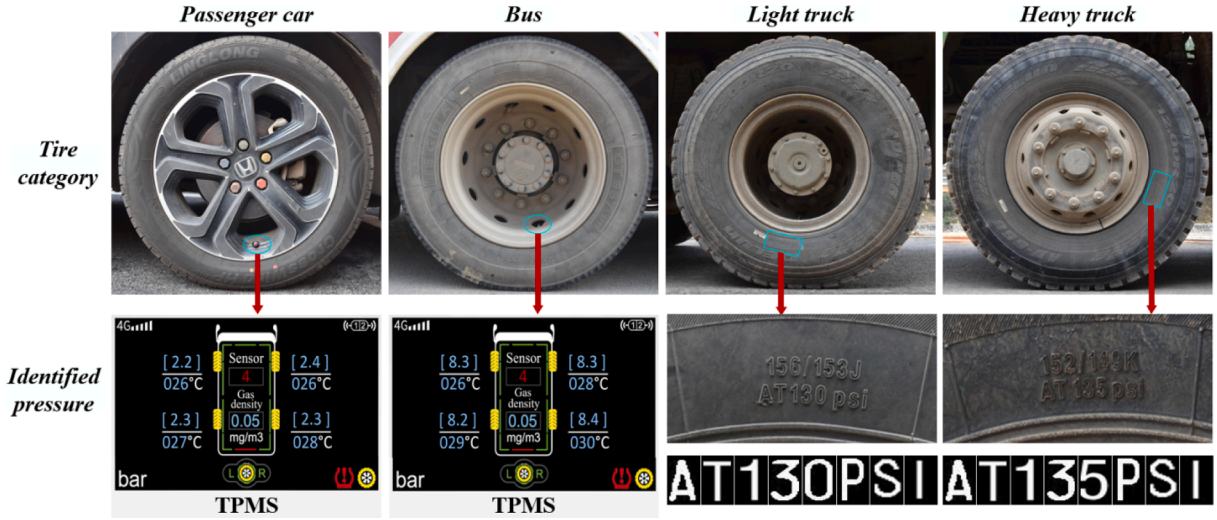

Fig. 12. Tire pressure identification.

lower boundaries of the characters are obtained by row scanning, and the left and right boundaries are obtained by column scanning. For an ideal image, the gray value of the white background is 255 and the gray value of the black characters is 0. It is also found that a threshold of 215 is sufficient to distinguish the background and the character. That is, the region with gray average smaller than 215 is defined as the character. By applying the window scanning algorithm on the image shown in Fig. 9(a), the characters of the tire size marking are divided into single characters, as shown in Fig. 9(b).

The final step is the character recognition, and the template matching algorithm as one of the most widely used method was adopted. By comparing the observed character with a set of character templates, a similarity measure is calculated and the identification of character is assigned with the most similar template character [44]. The matching result is shown in Fig. 9(c).

3.3. Identification of tire deformation

The first step for obtaining the tire deformation is to determine the scale factor of the image. In this study, it is assumed that the wheel rim is rigid without any deformation under the vertical load on the tire. Thus, the dimension of the rim could be used for image

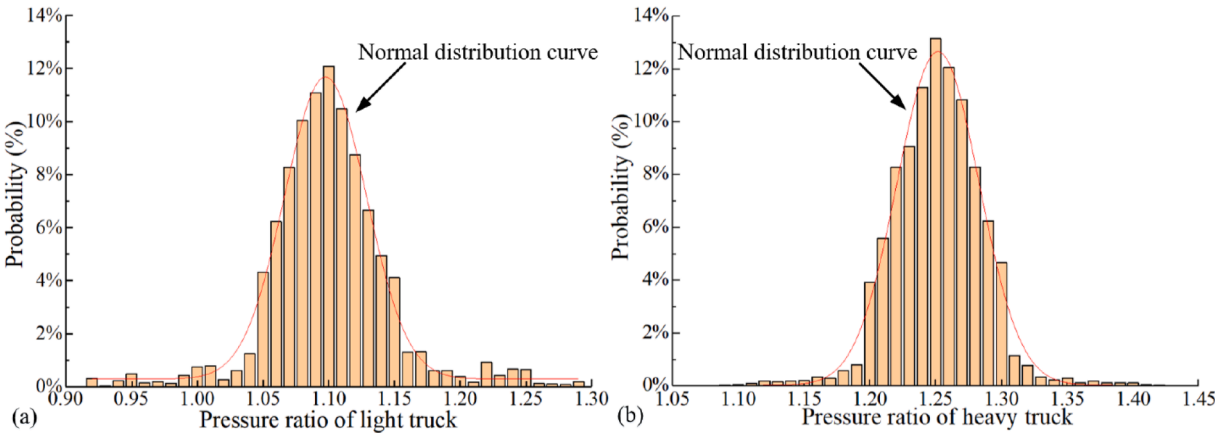

Fig. 13. Tire pressure ratio: (a) light trucks; (b) heavy trucks.

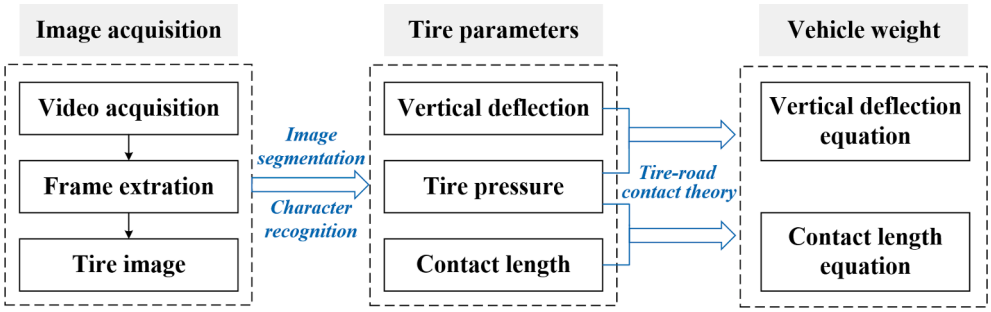

Fig. 14. Procedure of CV-based vehicle weighing.

calibration. Based on the application of image segmentation and character recognition techniques elaborated in the previous sections, the edges of the tire and the rim can be obtained as shown in Fig. 10, as well as the pixel number of those edges. Herein, the diameter of the rim in the picture has a pixel number of *M*. Meanwhile, based on the character recognition techniques, the designated diameter of the rim is 20 in. (508 mm) as shown on the sidewall. The scale factor of the image is then calculated as the ratio of the physical length to the pixels of the rim diameter, as shown in Fig. 10.

The calculation of tire deformation including the vertical deflection and contact length is shown in Fig. 11. In terms of the vehicle configuration, the vehicle weight is applied at the wheel center and transferred to the tire. Thus, it is assumed that the upper half tire above the rim center has no deformation. The upper half of the tire edge can be used to generate a complete circle serving as the intact tire edge without deformation. Then, the vertical deflection (i.e., the distance between the lowest points of the deformed tire edge and the complete circle) can be obtained by multiplying the number of vertical deflection pixels with the scale factor. Similarly, the contact length was calculated as shown in Fig. 11(b). The intersection points between the deformed tire edge and the complete circle are the contact edge points, i.e., point 1 and point 3 in the figure. As a result, the contact length is obtained by multiplying the number of contact length pixels with the scale factor.

3.4. Identification of tire pressure

The tire pressure can be easily measured using a variety of sensors, such as the tire pressure monitor system (TPMS) installed on most passenger cars and buses [45,46], as shown in Fig. 12. However, most trucks do not have the TPMS and it is difficult to measure the tire pressure during the vehicle moving. This study proposed a non-contact method to obtain the tire pressure. From the tire image, the tire pressure marking on the sidewall can be identified using the character recognition technique described above, as shown in Fig. 12. It is noted that the tire pressure labeled on the sidewall is the maximum allowed pressure for the tire, not the actual pressure of the tire. According to the research in the literature [47,48], some relationship may exist between the labeled pressure and the actual pressure in normal condition. Based on the statistical analysis of a large number of testing data measured by the authors, the probability distribution of the ratio between the measured pressure and the labeled pressure is shown in Fig. 13, which follows the normal distribution for both light trucks and heavy trucks. At 95% confidence level, for light trucks, the ratio is 1.05–1.15, while for heavy trucks it is 1.20–1.30. Herein, a ratio of 1.1 was assumed for the light truck and 1.25 for the heavy truck. Therefore, the actual value of tire pressure can be obtained by multiplying the ratio with the labeled tire pressure. It is also worth noting that the tire pressure will increase as the tire temperature increases when the vehicle is in motion. However, it is found that the effect of tire temperature increase

Fig. 15. SUV weighing test.

Table 1
Comparison of tire deflection results.

Location	Rim pixels	Scale factor	Deflection pixels	Predicted deflection (mm)	Measured deflection (mm)	e_{RE} (%)	Contact length pixels	Predicted contact length (mm)	Measured contact length (mm)	e_{RE} (%)
FL	2534	0.1904	79	15.04	15	0.28	884	168.31	170	−0.99
FR	2547	0.1895	75	14.21	14	1.52	863	163.54	168	−2.68
RL	2545	0.1896	55	10.43	10	4.28	691	131.01	127	3.16
RR	2527	0.1910	57	10.89	11	−1.03	702	134.08	136	−1.41

Note: e_{RE} denotes the relative error (%) between the predicted value and measured value.

on the vehicle weight identification is minor and could be ignored in this study.

3.5. Procedure of CV-based vehicle weighing

The overall procedure of the CV-based vehicle weight identification is presented in Fig. 14. First, a vision device such as the digital camera is used to capture the tire images of vehicles. Second, the image segmentation and character recognition techniques are applied to obtain the vertical deflection, contact length, and tire pressure. Third, the identified values are substituted into the newly derived theoretical models, i.e., the vertical deflection and inflation pressure into Eq. (15), or the contact length and inflation pressure into Eq. (16), to calculate the load sustained by each tire. Finally, the vehicle gross weight is obtained by summation of all the tire loads.

4. Verification of CV-based method

4.1. Verification of deformation measurement

The vertical deflection and contact length of the tire are essential parameters for the CV-based vehicle weight identification. In this section, a few tests were implemented to verify the proposed method for the tire deformation identification. The SUV as a typical and common vehicle type is selected for testing, as shown in Fig. 15. The weighing system consists of a camera (NikonD5600), tripod, tire pump, tire pressure sensor, carbon paper, and laptop. The notations for the tires are front left (FL), front right (FR), rear left (RL), and rear right (RR), and the measured tire loads are 5390 N, 5194 N, 3626 N, and 3724 N. The tire pressure measured by TPMS is 220 kPa. Table 1 shows the comparison of the predicted tire deflection based on CV method and the measured results using the rangefinder and carbon paper.

Take the front left (FL) wheel as an example to demonstrate the identification of the vertical deflection and contact length, as shown in Fig. 16. The rim diameter contains 2534 pixels in the image, while the physical value of rim diameter is 19 in. (508 mm) in terms of the size marking identified using character recognition. The scale factor of the tire image, the ratio of the physical length to the pixels of the rim diameter, is calculated as 0.1904. Based on the image segmentation, the vertical deflection is 79 pixels and the contact length is 884 pixels, which implies that the vertical deflection and contact length predicted by the computer vision method are 15.04 mm and

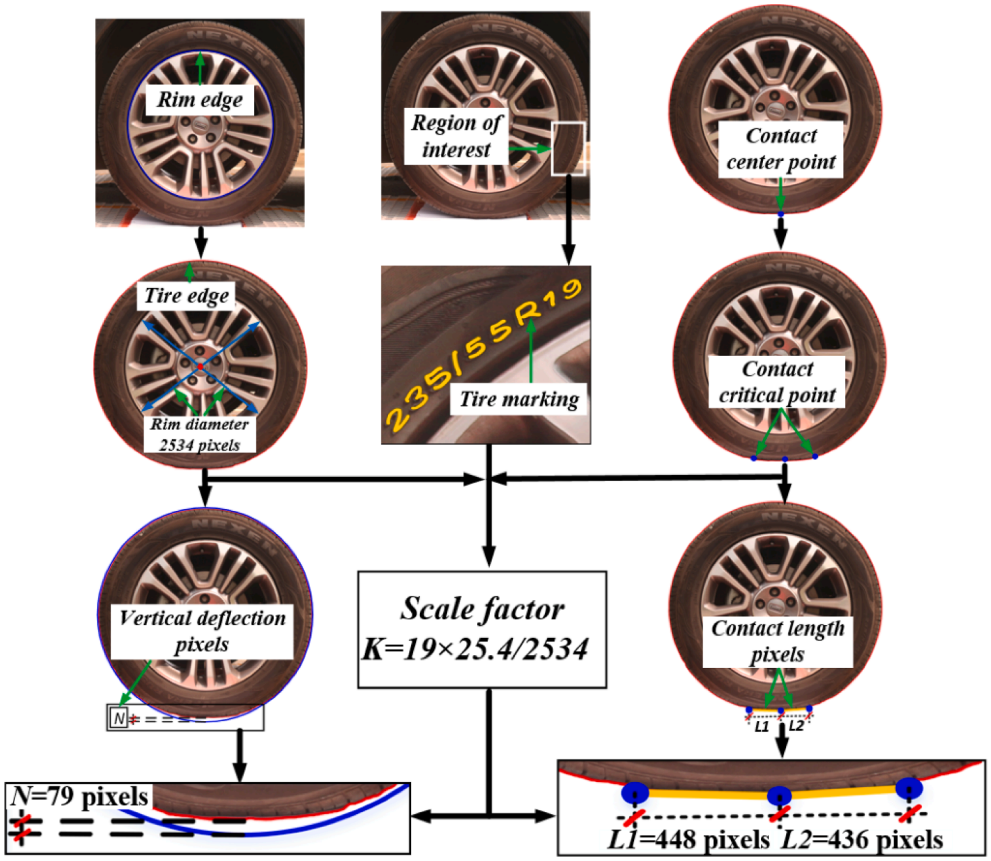

Fig. 16. Calculation of tire deformation.

168.31 mm, respectively. The vertical deflection value measured by laser rangefinder is 15 mm and the contact length value measured by carbon paper is 170 mm. The identification errors for the vertical deflection and contact length are 0.28% and −0.99%, respectively. The results of other tires are also presented in Table 1. From the Table 1, the results predicted by the CV-based method agree very well with the measured results, having errors within 5%, which indicates that the proposed CV-based method has a high accuracy.

4.2. Verification of contact area measurement

The contact length is a simple parameter to reflect the tire-road model, while the contact area is a better parameter with more information, which can also be used to verify the assumption of elliptical contact area in the theoretical model. A test followed the JTGE60-2008 specification [49] was conducted to obtain the contact footprint as shown in Fig. 17. The footprint image was pre-processed using Gaussian filtering to reduce noise and enhance the contrast of the image [50]. The image was then converted into a black and white binary image using the Otsu algorithm, where the nonzero elements in the binary image represent the actual tire contact area. Finally, the pixels of tire footprint in the binary image and the contact area were calculated.

The actual contact area is an irregular shape as can be seen in this figure. The previous research assumes the contact area as some simple shapes, such as rectangle, circle. Reference [53] calculates the contact area based on the vertical deflection and radius of the tire, while the present study adopts the oval shape for calculating the contact area. The equations of all the methods are listed in Table 2.

The results of the four tires are shown in Table 3. The average errors of the rectangular and circular methods are 9.31% and 9.24%, respectively. The deflection method does not require tire width and the average error is 7.46%. The average error of the oval method is only 0.74%. Therefore, among all the methods, the oval method has the best accuracy in calculating the contact area, which validates the assumption of elliptical contact shape.

4.3. Verification of inflation pressure measurement

A few tests were conducted to verify the identification of tire inflation pressure. The tested tire is 12.00R20 truck tire. Based on the developed character recognition technique, the labeled pressure was identified as 135 PSI (0.93 MPa), and the inflation pressure is then predicted as 1.16 MPa using the ratio of 1.25. 80 sets of tire pressures were measured to obtain the actual inflation pressure as

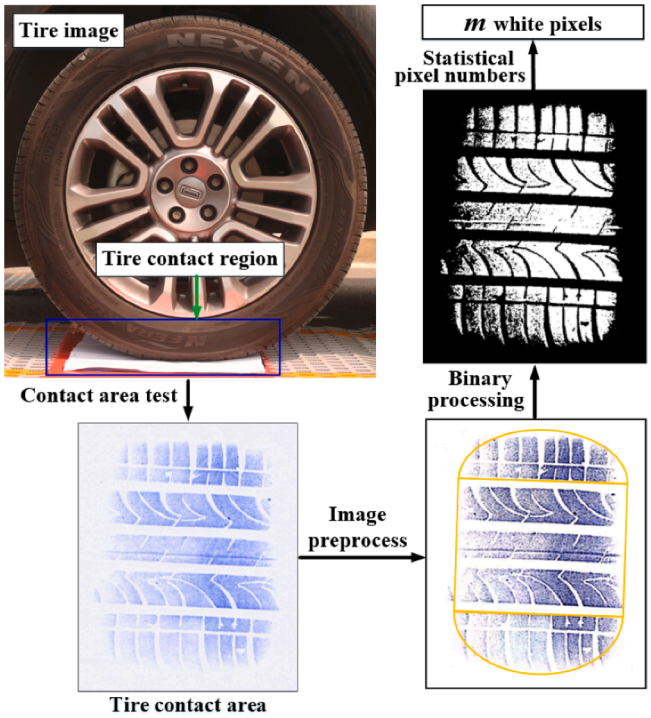

Fig. 17. Identification of contact area.

Table 2
Methods of calculating tire contact area.

Methods	Equations
Rectangular [51]	$S = 4a \times b$
Circular [52]	$S = \frac{a^2}{a^2+b^2} \times \pi(a)^2 + \frac{b^2}{a^2+b^2} \times \pi(b)^2$
Deflection [53]	$S = \pi \times f \times R$
Oval	$S = \frac{2}{3} \times 2a \times 2b + \frac{\pi}{3} \times a \times b$

Table 3
Comparison of contact area using different methods.

Method	FL		FR		RL		RR		e_{AVE} (%)
	Area (cm^2)	e_{RE} (%)	Area (cm^2)	e_{RE} (%)	Area (cm^2)	e_{RE} (%)	Area (cm^2)	e_{RE} (%)	
Footprint	189.73	–	185.55	–	128.85	–	135.32	–	–
Rectangular	208.17	9.72	201.3	8.49	140.73	9.22	148.61	9.82	9.31
Circular	167.83	−11.54	169.17	−8.83	118.21	−8.26	124.04	−8.34	−9.24
Deflection	171.80	−9.45	172.05	−7.28	120.57	−6.43	126.26	−6.70	−7.46
Oval	193.28	1.87	181.33	−2.27	130.67	1.41	137.97	1.96	0.74

Note: e_{AVE} denotes the average error (%) between the predicted values and measured values.

shown in Table 4. As seen in the table, the error between the measured pressure and the predicted pressure is within 10%, except for the only case with measured pressure of 1.02 MPa. In addition, for 75 of the measured data, the error of data is less than 5%. It shows that the CV-based identification of tire inflation pressure has a good accuracy.

5. Comparison of vehicle weighing methods

5.1. Results of different equations

There are two ways to determine the vehicle weight based on the available tire deformation and pressure, that is, one way is to use

Table 4
Results of measured inflation pressures.

Measured pressure (MPa)	1.02	1.09	1.10	1.11	1.12	1.13	1.14	1.15	1.16	1.17	1.18	1.19	1.20	1.21	1.22	1.26
e_{RE} (%)	−12.3	−6.74	−5.77	−4.82	−3.88	−2.96	−2.06	−1.17	0	0.56	1.4	2.23	3.04	3.84	4.63	8.0
Number of occurrences	1	2	1	3	4	8	7	8	11	9	8	6	5	4	2	1
Percentage (%)	1.25	2.5	1.25	3.75	5	10	8.75	10	13.75	11.25	10	7.5	6.25	5	2.5	1.25

Table 5
Measured information for comparison.

Tire type	Vertical deflection (mm)	Contact length (cm)	Pressure (kPa)	Weight (N)
SUV tire	15.06	16.24	220	5488
Truck tire	25.85	22.23	1015	35,084

the vertical deflection and tire pressure in terms of Eq. (15), and the other way is to use the contact length and tire pressure in terms of Eq. (16). Meanwhile, Peng et al. [54] established a semi-empirical equation between the load and the vertical deflection using measured data, here termed as Peng equation, as shown in Eq. (19). Feng et al. [27,28] calculated the vertical load by multiplying the inflation pressure with the contact area (assumed as a rectangular area), termed as Feng equation, as shown in Eq. (20).

$$f = \left[1 - \sqrt{1 - \left(\frac{F}{2bRP} \cdot \beta\right)^2}\right] R \tag{19}$$

$$F = PA = 4Pab \tag{20}$$

where A is tire-road contact area, $\beta = \lambda e^{\theta F/bRp}$ is stiffness factor, λ and θ are the empirical coefficients related to the vehicle type. The Eq. (19) was used to compare with Eq. (15), and the Eq. (20) was used to compare with Eq. (16). Herein, tires of SUVs and trucks were selected to evaluate the accuracy of these vehicle weighing equations. Table 5 lists the measured values including the tire deformation, tire pressure, and tire load.

By substituting the measured values into Eqs. (15), (16), (19), and (20), the results are shown in Table 6. As shown in Table 6, the identification errors of the proposed equations are much smaller than that of equations in the literature. The Peng equation is an empirical equation based on limited data and it has limited applicability. Feng equation assumed that the tire-road contact pressure is equal to the inflation pressure, which is not true for most situations. This is because the contact pressure of the vehicle varies greatly with the inflation pressure and vehicle weight [55].

For a reasonable comparison, 100 sets of SUV tires and 80 sets of truck tires were analyzed to compare the average error and standard deviation as shown in Table 7. The average errors of the Eqs. (15) and (16) are smaller than 6%. The results show that the weight of SUVs and trucks can be well identified using the proposed equations.

Table 6
Results of different equations.

Method	Equation	SUV		Truck	
		Force (N)	e_{RE} (%)	Force (N)	e_{RE} (%)
Vertical deflection method	Eq. (15)	5238.24	−4.55	37345.68	6.45
	Peng equation	3685.88	–32.84	29457.47	−16.04
Contact length method	Eq. (16)	5129.19	−6.54	31683.15	−9.69
	Feng equation	4604.04	−16.11	46255.07	31.84

Table 7
Error average and standard deviation of different equations.

Method	Equation	SUV		Truck	
		e_{AVE} (%)	σ_{SD} (%)	e_{AVE} (%)	σ_{SD} (%)
Vertical deflection method	Eq. (15)	3.83	3.43	4.69	3.55
	Peng equation	24.77	4.24	15.75	6.84
Contact length method	Eq. (16)	5.75	3.96	7.67	4.77
	Feng equation	14.73	6.41	22.34	6.91

Note: σ_{SD} denotes the standard deviation (%) between the predicted values and measured values.

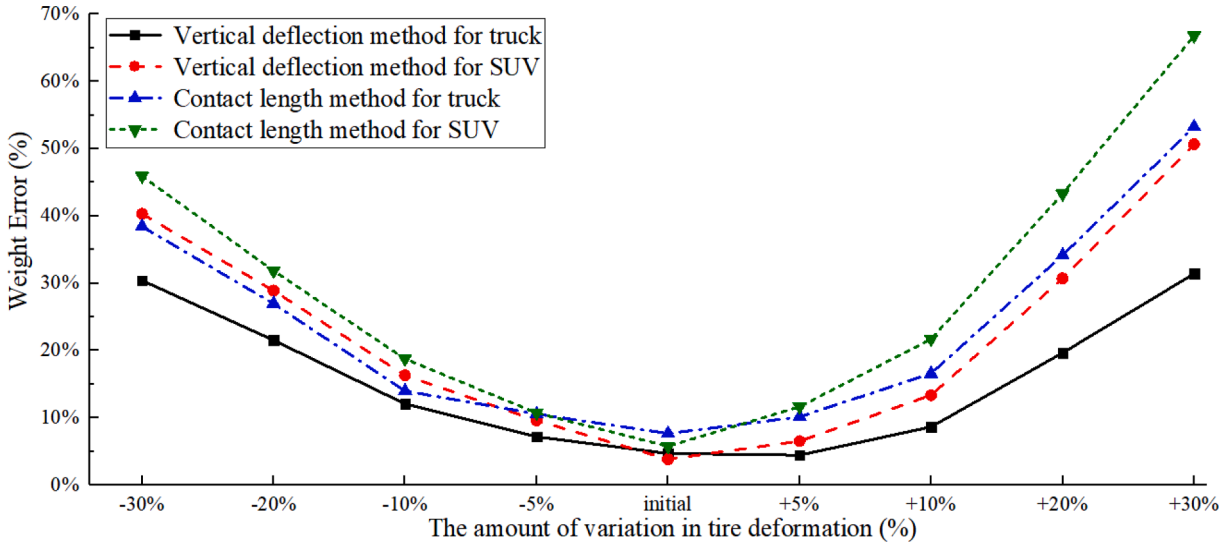

Fig. 18. Vehicle weight identification error.

5.2. *Sensitivity analysis*

To study the sensitivity of tire deformation on vehicle weight identification, the above 180 sets of tire deformation are changed to simulate the measurement error. A variation of −30% to 30% is introduced in the measured tire vertical deflection and contact length. The identification errors of Eqs. (15) and (16) are compared as shown in Fig. 18. It is found that the error of the contact length method is larger than the result of the vertical deflection method, which could be due to that Eq. (16) contains the second power of the contact length *a,* while Eq. (15) contains the first power of vertical deflection *f*. Thus, it implies that the vertical deflection method in Eq. (15) has a better performance on the vehicle weight identification.

6. Field tests

The proposed CV-based vehicle weighing method, which was verified with experimental results and compared with other methods in the previous sections, shows a good performance. In this section, several field tests were conducted to study the robustness of the proposed method in various conditions.

6.1. *Identification of SUV weight*

The performance of the proposed method was tested on a SUV. To further verify the accuracy of the present weighting identification method, the tire pressure is increased from 180 to 260 kPa with an interval of 20 kPa. The actual weights of the FL tire and the RL tire are 4998 N and 4067 N, respectively. As shown in Table 8, the deformations of FL and RL tires tend to decrease with the increase of pressure. When the pressure changes from 180 kPa to 260 kPa, the deformation of the FL tire decreases more than that of the RL tire, which indicates that the tire with heavier loads produces more deformation.

The identification errors of the SUV weight under different tire pressures are shown in Fig. 19. When the pressures are in the range of 200 kPa to 240 kPa, the errors of axle load and gross weight are within 5%. The tire deformation under low-pressure 180 kPa is large, and the mechanics of the tire is in the state of elastic–plastic large-deformation, which is the reason for the large error. The tire deformation under high-pressure 260 kPa is small, and the small change from the deformation could also magnify the identified error.

Table 8
Comparison of SUV weight under different tire pressures.

Pressure (kPa)	FL tire				RL tire			
	Vertical deflection method		Contact length method		Vertical deflection method		Contact length method	
	Vertical deflection (mm)	Force (N)	Contact length (cm)	Force (N)	Vertical deflection (mm)	Force (N)	Contact length (cm)	Force (N)
180	16.79	5382	17.98	5389	14.41	4282	16.54	4394
200	15.18	5147	16.62	5116	12.92	4056	15.39	4225
220	14.16	5115	15.50	4895	11.85	3942	14.67	4220
240	12.90	4881	14.62	4750	11.01	3877	13.65	3985
260	11.91	4724	13.91	4659	10.13	3739	12.76	3772

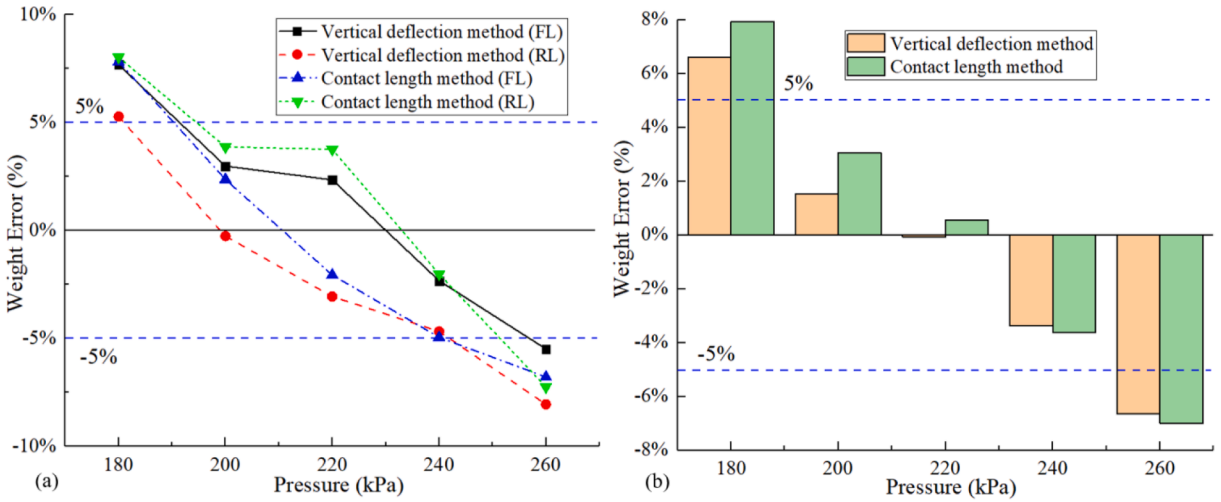

Fig. 19. SUV weight identification error: (a) axle load; (b) gross weight.

Table 9
Comparison of SUV weight under different weights.

Weight (N)	Weight distribution (N)	Measured weight (N)	Identified force from vertical deflection (N)	e_{RE} (%)	Identified force from contact length (N)	e_{RE} (%)
Empty	FL	5439	5288	−2.78	5277	−2.98
	RL	3871	4009	3.56	3679	−4.96
	Gross weight	18,620	18,594	−0.14	17,912	−3.80
Fully loaded	FR	5880	5948	1.16	5771	−1.85
	RR	4998	5142	2.88	5183	3.70
	Gross weight	21,756	22,180	1.95	21,908	0.70

In addition, the error of Eq. (15) is smaller than that of Eq. (16).

To study the effect of vehicle load on the CV-based weight identification, the vehicle loads are changed by increasing the number of passengers. The sum of vehicle weight and driver weight is 18620 N as the initial load of the vehicle. After adding 5 people, the gross weight reaches 21756 N. Additionally, the pressures are kept at 220 kPa by TPMS. The identified weight results of SUV under different weights are shown in Table 9. The identified errors of Eqs. (15) and (16) decrease with the increase of vehicle weight. The two equations can well identify SUV weight, and both errors are within 5%. However, the identified error of the vertical deflection method is smaller than that of the contact length method. Therefore, it is suggested to use the vertical deflection method to identify SUV weight in applications.

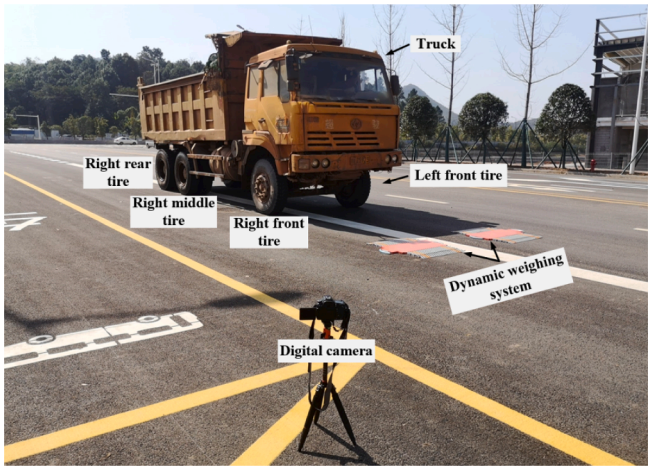

Fig. 20. Truck weighing test.

Table 10
Comparison of tire deformation between empty and full-load.

Tire	Empty (N)	Loaded (N)	Empty	Loaded	Difference (mm)	Empty	Loaded	Difference (cm)
			Vertical deflection (mm)			Contact length (cm)		
Front	29,925	32,037	20.91	21.36	0.45	20.20	21.61	1.42
Middle	31,648	63,945	12.19	21.76	9.57	14.59	21.69	7.10
Rear	32,626	68,061	12.55	22.83	10.28	14.82	22.26	7.44

Table 11
Comparison of truck weight between empty and full-load.

Vehicle load status	Distribution	Measured weight (N)	Identified force of vertical deflection (N)	e_{RE} (%)	Identified force of contact length (N)	e_{RE} (%)
Empty	Front Wheel	29,925	30,851	3.09	28,752	−3.92
	Middle Wheel	31,648	30,623	−3.24	30,022	−5.14
	Rear Wheel	32,626	31,785	−2.58	30,976	−5.06
	Gross weight	188,398	186,516	−1.00	179,499	−4.72
Fully loaded	Front Wheel	32,037	31,741	−0.92	32,928	2.78
	Middle Wheel	63,945	65,064	1.75	66,349	3.76
	Rear Wheel	68,061	69,384	1.94	69,885	2.68
	Gross weight	328,086	332,377	1.31	338,324	3.12

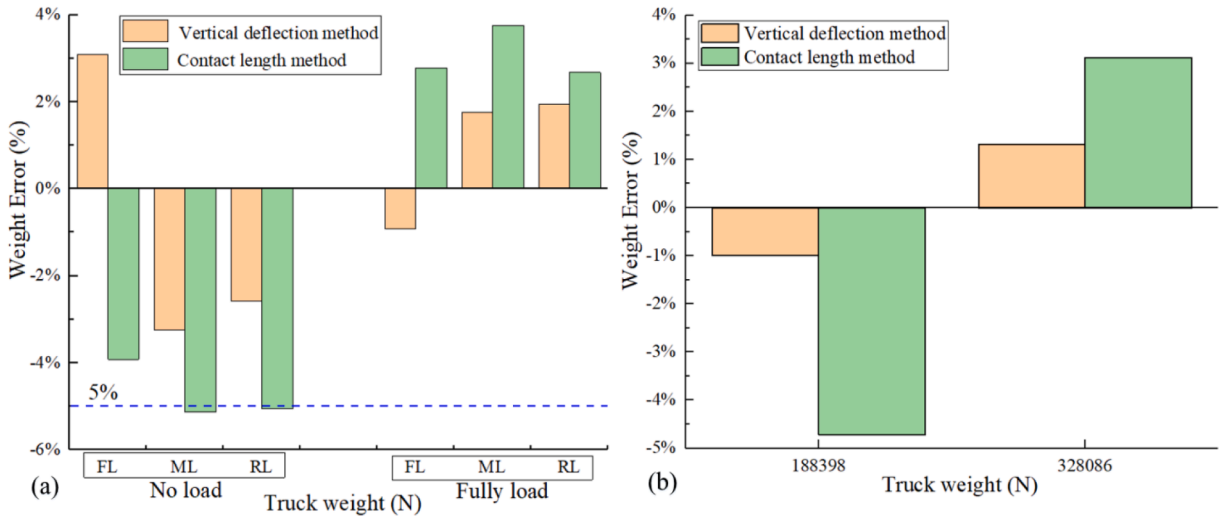

Fig. 21. Truck weight identification error: (a) axle load; (b) gross weight.

6.2. *Identification of truck weight*

Heavy trucks were also tested in the construction site, as shown in Fig. 20. The truck weight at empty state is 188398 N and 328086 N at fully-loaded state. The deformation of the front, middle, and rear tires are measured using CV as shown in Table 10. For the front tire, the vertical deflection and the contact length between the empty and full-load cases are very close, which is because that the majority of vehicle weight is on the middle and rear tires.

The CV-based measured vertical deflection and the contact length are used to obtain the truck weights of the empty and fully-loaded states, as shown in Table 11. Compared with the contact length method, the identified weights of the vertical deflection method are closer to the measured value, but the identified weights by both methods can reach a high level of reliability for the truck weight identification.

To compare the accuracy under different truck weights, Eqs. (15) and (16) are used to evaluate the error of truck axle weight and gross weight, as shown in Fig. 21. For Eqs. (15) and (16), the errors decrease with the increase of vehicle weight, and the errors are within 4% and 6%, respectively. Furthermore, the CV-based vehicle weighing methods can more accurately identify the loaded trucks than the empty ones. Therefore, the CV-based vehicle weighing methods have contributed to monitor the loading capacity of trucks.

To study the accuracy of the CV-based identified truck weight in different motion states, the truck was first stopped on the portable

Table 12
Comparison of truck weight under different motion states.

Vehicle weight distribution	Static weight (N)	Dynamic weight (N)	e_{RE} (%)
Front Wheel	35,329	33,722	−4.55
Middle Wheel	75,019	73,892	−1.50
Rear Wheel	73,353	71,589	−2.41
Gross weight	367,402	358,406	−2.45

Table 13
Comparison of truck weight for multiple-trucks.

Distribution	Truck - ZHE H. N1933			Truck - ZHE H. 28,590			Truck -ZHE H. B3098		
	Measured (N)	Identification (N)	e_{RE} (%)	Measured (N)	Identification (N)	e_{RE} (%)	Measured (N)	Identification (N)	e_{RE} (%)
Front	41,209	42,182	2.36	41,111	42,254	2.78	44,737	43,775	−2.15
Middle	77,812	75,438	−3.05	88,396	87,406	−1.12	80,654	82,759	2.61
Rear	79,331	77,229	−2.65	76,979	79,596	3.40	72,618	75,595	4.10
Gross weight	396,704	389,698	−1.77	412,972	418,512	1.34	396,018	404,258	2.08

weighing device that recorded the static weight of the truck. The tire traveling at 20 km/h is captured by the digital camera and the tire images of each frame are input into the CV-based weight identification method. Finally, the dynamic weight of the truck can be consequently identified, and the results are shown in Table 12. It indicates that the difference of tire load between static and motion states is small, and the maximum errors of the two states are within 5%, but the vertical loads of the front, middle, and rear wheels in motion state are smaller than that in the static state. The centrifugal force generated by the tire rotation uplifts the gravity center of the truck, which reduces the contact length and vertical deflection, and underestimates the vehicle weight when using Eqs. (15) and (16).

Numerous field tests were conducted on the weight of multiple-trucks to further evaluate the accuracy by using Eq. (15). The comparison of identified weight for multiple-trucks is shown in Table 13. The identified weights of the truck are consistent with the measured data, the errors decrease with the increase of the truck weights, and the error is within 5%. According to the identified errors for multiple-trucks, the CV-based weight identification method can accurately obtain the weight of multiple-trucks, which is applied in practical applications.

7. Conclusions

This study proposed a non-contact vehicle weight identification method based on the tire-road contact model and computer vision techniques. The theoretical model of tire-road contact was established based on the improved Hertz contact theory. Computer vision techniques including the image segmentation and character recognition were adopted for the identification of tire deformation and inflation pressure. Field tests on passenger cars and trucks were conducted to verify the proposed method. The following conclusions can be drawn:

(1) The Hertz contact theory was improved to derive the theoretical model of tire-road contact by integrating the geometric, equilibrium, and physical equations. With that, the relationship between the vertical force, tire deformation, and inflation pressure was established, which provides the basis for vehicle weight identification.
(2) The methodology of computer vision-based vehicle weighing was developed. That is, the image segmentation algorithm was used to automatically extract the edges of tire and rim. The character recognition algorithm was adopted for the character detection in the tire sidewall image. In addition, the general procedure to identify the tire deformation and inflation pressure from the image using the computer vision methods was developed.
(3) A few tests on the SUV were implemented to verify the CV-based identification of tire vertical deflection and contact length. The results show that the vertical deflection and contact length predicted by the CV-based method agree very well with the measured results, having errors within 5%, The result of contact area also validates that the assumption of elliptical contact shape.
(4) There are two ways to determine the vehicle weight based on the developed weight equation and the available tire information, that is, one way is to use the vertical deflection and tire pressure, and the other way is to use the contact length and tire pressure. The comparison results show that the proposed method has higher accuracy than the methods in literature, and the method using tire deflection is better than the method using contact length
(5) Field tests on the SUVs and trucks were conducted to study the robustness of the proposed method in various conditions, including the effects of inflation pressure, vehicle weight, motion state, and tire type. The results show that the inflation pressure and vehicle weight have a significant effect on the identification error; however, the maximum identification error of the vehicle weight is within 10%, which indicates that the proposed method has a robust performance.

The non-contact vehicle weighing method has the advantages of high accuracy, long service life, and easy installation. In addition,

the proposed weighing system costs less than the three systems (static weighing, PWIM, and BWIM). This system is a supplementary method to obtain the vehicle weight and overcomes the disadvantages of the traditional weighing system. Although the proposed method shows a good performance, many uncertain factors, such as the camera vibration, shooting environment, and vehicle driving condition, could affect the identification accuracy in the practical application. For example, the camera vibration would cause image distortion, lighting conditions (low light, shadows) would make it difficult to recognize the edge of the tire image, and high-speed vehicles could easily produce blurry tire images. Therefore, further research is conducting to improve the applicability of the proposed method in a complex environment.

Declaration of Competing Interest

The authors declare that they have no known competing financial interests or personal relationships that could have appeared to influence the work reported in this paper.

Acknowledgements

This research work was fully supported by the National Natural Science Foundation of China (Project No. 52008160), Excellent Young Scholars Fund of Hunan Province (Project No: 2021JJ20015), the Postgraduate Scientific Research Innovation Project of Hunan Province (Project No: CX20200405).

Appendix A. The equivalent elastic modulus

The equivalent elastic modulus of the tire-road at the contact area is expressed,

$$\frac{1}{E_e} = \frac{(1-\lambda_t^2)}{E_t} + \frac{(1-\lambda_r^2)}{E_r} \tag{A.1}$$

where E_e is the equivalent elastic modulus, E_t and λ_t are the elastic modulus and Poisson's ratio of the tire, respectively. E_r and λ_r are the elastic modulus and Poisson's ratio of the road, respectively. The road elastic modulus ranges from 800 to 1200 MPa, while the maximum elastic modulus of truck tires is 1.5 MPa. The road deformation is much smaller than the tire deformation. It is reasonable to assume the road as a rigid body in the road-tire contact model. Thus, the equivalent Poisson's ratio λ_e is equal to λ_t and the Eq. (A.1) can be simplified as:

$$E_e = \frac{E_t}{1-\lambda_e^2} \tag{A.2}$$

The equivalent Poisson's ratio λ_e in Eq. (A.2) can be obtained as follows.
As shown in Fig. 1, the equivalent strain of the tire in the vertical direction is,

$$\varepsilon_{OB} = \frac{OC}{O'C} = \frac{f}{R} \tag{A.3}$$

Meanwhile, the equivalent strain in the horizontal direction is calculated as,

Table A1
The coefficient of different tire types.

Diagonal tire	Car	Light truck	Bus	Heavy truck
Coefficient α	1.1	1.1	1.2	1.2
Radial tire	Car	Light truck	Bus	Heavy truck
Coefficient α	1	1	1.1	1.1

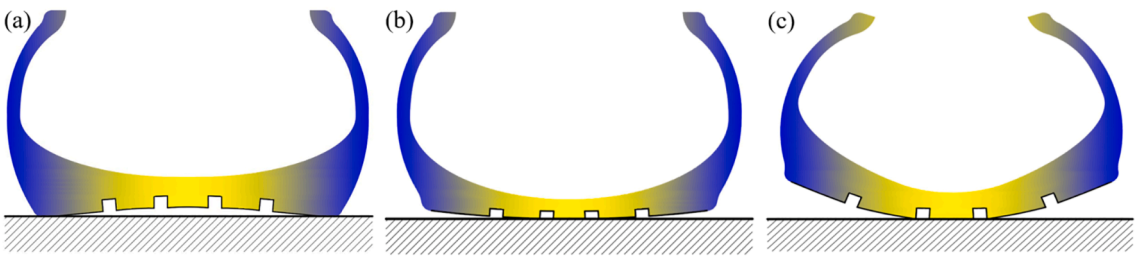

Fig. A1. The tire sections under different pressure conditions: (a) underpressure; (b) normal pressure; (c) overpressure.

$$\varepsilon_{AO} = \frac{AC - AO}{AC} = \frac{R\theta - \sqrt{2Rf - f^2}}{R\theta} \tag{A.4}$$

Then, the equivalent Poisson's ratio λ_e is calculated as,

$$\lambda_e = \frac{\varepsilon_{AO}}{\varepsilon_{OB}} = \frac{R\theta - \sqrt{2Rf - f^2}}{R\theta} \times \frac{R}{f} \tag{A.5}$$

Since θ is relatively small, it can be simplified as:

$$\theta = arcsin\frac{\sqrt{2Rf - f^2}}{R} \approx \frac{\sqrt{2Rf - f^2}}{R} + \frac{1}{6}\left(\frac{\sqrt{2Rf - f^2}}{R}\right)^3 \tag{A.6}$$

By substituting Eq. (A.6) into Eq. (A.5), we have,

$$\lambda_e = \frac{\varepsilon_{AO}}{\varepsilon_{OB}} = \frac{2Rf - f^2}{6R^2 + 2Rf - f^2} \tag{A.7}$$

In Eq. (A.2), the elastic modulus of the tire is mainly affected by the inflation pressure. The tire types are divided into eight categories in terms of tire size markings and usages as shown in Table A1 [45,46]. The relationship between the elastic modulus and the pressure is as follows [56,57]:

$$E_t = \gamma \cdot \alpha \cdot p \tag{A.8}$$

where α is the coefficient of different tire types, as shown in Table A1; and γ is the influence coefficient of tire radius, and the detailed values are shown below.

The actual radius of the tire varies with tire pressure. Fig. A1 shows the tire sections under three conditions of tire pressure: underpressure, normal pressure, and overpressure [56]. As can be seen, the contact area will increase or decrease due to the change of tire inflation pressure. Based on previous studies in literature, the influence coefficient of tire radius γ can reflect the change of contact area with tire pressure [57,58]. $\gamma = 1.25$ for underpressure case, $\gamma = 1$ for normal pressure case, and $\gamma = 0.75$ for overpressure case.

References

[1] Z. Chen, T.H.T. Chan, A. Nguyen, Y. Ling, Identification of vehicle axle loads from bridge responses using preconditioned least square QR-factorization algorithm, Mech. Syst. Signal Process. 128 (2019) 479–496, https://doi.org/10.1016/j.ymssp.2019.03.043.

[2] B.F. Spencer, V. Hoskere, Y. Narazaki, Advances in computer vision-based civil infrastructure inspection and monitoring, Engineering 5 (2) (2019) 199–222, https://doi.org/10.1016/j.eng.2018.11.030.

[3] R. Hou, S. Jeong, J.P. Lynch, M. Ettouney, K.H. Law, Data-driven analytical load rating method of bridges using integrated bridge structural response and weigh-in-motion truck data, Mech. Syst. Signal Process. 163 (2022) 108–128, https://doi.org/10.1016/j.ymssp.2021.108128.

[4] B. Jacob, V. Feypell-de La Beaumelle, Improving truck safety: potential of weigh-in-motion technology, IATSS Research. 34 (1) (2010) 9–15, https://doi.org/10.1016/j.iatssr.2010.06.003.

[5] H. Rakha, B. Katz, A. Al-Kaisy, Field evaluation of truck weigh station operations, J. Intelligent. Trans. Syst. 10 (2) (2006) 49–57, https://doi.org/10.1080/15472450600626224.

[6] T.H.T. Chan, L. Yu, S.S. Law, T.H. Yung, Moving force identification studies, I: theory, J. Sound Vib. 247 (1) (2001) 59–76, https://doi.org/10.1006/jsvi.2001.3630.

[7] M. Sujon, F. Dai, Application of weigh-in-motion technologies for pavement and bridge response monitoring: state-of-the-art review, Auto. Construct. 130 (2021) 103844, https://doi.org/10.1016/j.autcon.2021.103844.

[8] J. Gajda, P. Burnos, R. Sroka, Accuracy assessment of weigh-in-motion systems for vehicle's direct enforcement, IEEE. Intelligent. Trans. Syst. Magazine. 10 (2018) 88–94. https://ieeexplore.ieee.org/document/8263437.

[9] C. Liu, D. Huang, T.-L. Wang, Analytical dynamic impact study based on correlated road roughness, Computers. Struct. 80 (20-21) (2002) 1639–1650, https://doi.org/10.1016/S0045-7949(02)00113-X.

[10] P. Burnos, D. Rys, The effect of flexible pavement mechanics on the accuracy of axle load sensors in vehicle weigh-in-motion systems, Sensors. 17 (2017) 2053, https://doi.org/10.3390/s17092053.

[11] D. Cantero, Moving point load approximation from bridge response signals and its application to bridge weigh-in-motion, Eng. Struct. 233 (2021) 111931, https://doi.org/10.1016/j.engstruct.2021.111931.

[12] F. Moses, Weigh-in-Motion system using instrumented bridges, J. Transp. Eng. ASCE. 105 (3) (1979) 233–249, https://doi.org/10.1061/TPEJAN.0000783.

[13] J. Richardson, S. Jones, A. Brown, E. O', N.A. Brien, D. Hajializadeh, On the use of bridge weigh-in-motion for overweight truck enforcement, Inter. J. Heavy. Vehicle. Syst. 21 (2) (2014) 83, https://doi.org/10.1504/IJHVS.2014.061632.

[14] Y. Yu, C.S. Cai, L.u. Deng, State-of-the-art review on bridge weigh-in-motion technology, Adv. Struct. Eng. 19 (9) (2016) 1514–1530, https://doi.org/10.1177/1369433216655922.

[15] A.J. Cardini, J.T. DeWolf, Implementation of a long-term bridge weigh-in-motion system for a steel girder bridge in the interstate highway system, J. Bridge Eng. 14 (6) (2009) 418–423, https://doi.org/10.1061/(ASCE)1084-0702(2009)14:6(418).

[16] T. Ojio, K. Yamada, M. Wakao, Bridge weigh-in-motion using reaction force and analysis of traffic load characteristics, J. Struct. Eng. 49 (2003) 743–753.

[17] W. He, L.u. Deng, H. Shi, C.S. Cai, Y. Yu, Novel Virtual Simply Supported Beam Method for Detecting the Speed and Axles of Moving Vehicles on Bridges, J. Bridge Eng. 22 (4) (2017) 04016141, https://doi.org/10.1061/(ASCE)BE.1943-5592.0001019.

[18] W. He, T. Ling, E.J. OBrien, L.u. Deng, Virtual Axle Method for Bridge Weigh-in-Motion Systems Requiring No Axle Detector, J. Bridge Eng. 24 (9) (2019) 04019086, https://doi.org/10.1061/(ASCE)BE.1943-5592.0001474.

[19] Z. Chen, H. Li, Y. Bao, N.a. Li, Y. Jin, Identification of spatio-temporal distribution of vehicle loads on long-span bridges using computer vision technology, Struct. Control. Health. Monit. 23 (3) (2016) 517–534, https://doi.org/10.1002/stc.1780.

[20] D.H. Dan, L.F. Ge, X.F. Yan, Identification of moving loads based on the information fusion of weigh-in-motion system and multiple camera machine vision, Measurement 144 (2019) 155–166, https://doi.org/10.1016/j.measurement.2019.05.042.
[21] L. Ge, D. Dan, H. Li, An accurate and robust monitoring method of full-bridge traffic load distribution based on YOLO-v3 machine vision, Struct. Control. Health. Monitoring. 27 (12) (2020), https://doi.org/10.1002/stc.2636.
[22] T. Ojio, C.H. Carey, E.J. OBrien, C. Doherty, S.E. Taylor, Contactless bridge weigh-in-motion, J. Bridge Eng. 21 (7) (2016) 04016032, https://doi.org/10.1061/(ASCE)BE.1943-5592.0000776.
[23] M. Lydon, S.E. Taylor, D. Robinson, A. Mufti, E.J.O. Brien, Recent developments in bridge weigh in motion (B-WIM), J. Civil. Struct. Health. Monitoring. 6 (1) (2016) 69–81, https://doi.org/10.1007/s13349-015-0119-6.
[24] X.D. Jian, Y. Xia, J.A. Galant, L.M. Sun, Traffic sensing methodology combining influence line theory and computer vision techniques for girder bridges, J. Sensors. 1 (2019) 1–15, https://doi.org/10.1155/2019/3409525.
[25] Y. Xia, X.D. Jian, B. Yan, D. Sun, Infrastructure safety oriented traffic load Monitoring using multi-sensor and single camera for short and medium span bridges, Remote. Sensing. 11 (2019) 1–21, https://doi.org/10.3390/rs11222651.
[26] C.-Z. Dong, S. Bas, F.N. Catbas, A portable monitoring approach using cameras and computer vision for bridge load rating in smart cities, J. Civil. Struct. Health. Monitoring. 10 (5) (2020) 1001–1021, https://doi.org/10.1007/s13349-020-00431-2.
[27] M.Q. Feng, R.Y. Leung, C.M. Eckersley, Non-Contact vehicle weigh-in-motion using computer vision, Measurement 153 (2020) 107415, https://doi.org/10.1016/j.measurement.2019.107415.
[28] M.Q. Feng, R.Y. Leung, Application of computer vision for estimation of moving vehicle weight, IEEE. Sensors. J. 21 (2020) 11588–11597, https://doi.org/10.1109/JSEN.2020.3038186.
[29] P.S. Anoop, P. Nair, V. Sugumaran, Influence of unbalance on classification accuracy of tyre pressure monitoring system using vibration signals, Struct. Durability Health Monit. 15 (2021) 261–279, https://doi.org/10.32604/sdhm.2021.06656.
[30] K.L. Johnson, in: Contact mechanics, Cambridge University Press, Cambridge, 1987, pp. 99–104, https://doi.ISBN 0521 34796 3.
[31] A.-M. Wazwaz, Multiple-soliton solutions for the Boussinesq equation, Appl. Math. Comput. 192 (2) (2007) 479–486, https://doi.org/10.1016/j.amc.2007.03.023.
[32] H. Nakashima, A. Oida, Algorithm and implementation of soil-tire contact analysis code based on dynamic FE–DE method, J. Terramechanics. 41 (2-3) (2004) 127–137, https://doi.org/10.1016/j.jterra.2004.02.002.
[33] J. Prezelj, J. Murovec, S. Huemer-Kals, K. Häsler, P. Fischer, Identification of different manifestations of nonlinear stick–slip phenomena during creep groan braking noise by using the unsupervised learning algorithms k-means and self-organizing map, Mech. Syst. Signal Process. 166 (2022) 108349, https://doi.org/10.1016/j.ymssp.2021.108349.
[34] O. Loyola-Gonzalez, Black-Box vs. White-Box: Understanding Their Advantages and Weaknesses From a Practical Point of View, IEEE Access 7 (2019) 154096–154113.
[35] T.Y. Deo, A.D. Patange, S.S. Pardeshi, R. Jegadeeshwaran, A.N. Khairnar, H.S. Khade, A white-box SVM framework and its swarm-based optimization for supervision of toothed milling cutter through characterization of spindle vibrations, arXiv. 2112 (08421) (2021), https://doi.org/10.48550/arXiv.2112.08421.
[36] A.D. Patange, R. Jegadeeshwaran, Application of Bayesian family classifiers for cutting tool inserts health monitoring on CNC milling, International Journal of Prognostics and Health, Management. 11 (2020) 1–13, https://doi.org/10.36001/ijphm.2020.v11i2.2929.
[37] C. Revol, M. Jourlin, A new minimum variance region growing algorithm for image segmentation, Pattern Recogn. Lett. 18 (3) (1997) 249–258, https://doi.org/10.1016/S0167-8655(97)00012-3.
[38] Y. Dong, M. Liao, X. Zhang, F. Wang, Faults diagnosis of rolling element bearings based on modified morphological method, Mech. Syst. Signal Process. 25 (4) (2011) 1276–1286, https://doi.org/10.1016/j.ymssp.2010.10.008.
[39] W. Phornphatcharaphong, N.E. Anant, Edge-based color image segmentation using particle motion in a vector image field derived from local color distance images, J. Imaging. 6 (2020) 53–72, https://doi.org/10.3390/jimaging6070072.
[40] R.B. Chen, Y.F. Luo, An improved license plate location method based on edge detection, Physics Procedia 24 (2012) 1350–1356, https://doi.org/10.1016/j.phpro.2012.02.201.
[41] F. Albu, D. Hagiescu, M. Puica, L. Vladutu, Intelligent tutor for first grade children's handwriting application, Proceedings of the International Technology, Education and Development Conference. (2015) 3708-3717, https://doi.org/10.1.1.716.6559.
[42] F. Albu, Low complexity image registration techniques based on integral projections, in: International Conference on Systems, Signals and Image Processing (IWSSIP), 2016, pp. 1–4, https://doi.org/10.1109/IWSSIP.2016.7502708.
[43] R.K. Khamdamov, H.E. Rakhmanov, A character segmentation algorithm for vehicle license plates, Cybernetics. Syst, Analysis. 55 (4) (2019) 649–654, https://doi.org/10.1007/s10559-019-00173-0.
[44] S. Wang, H. Wang, Y. Zhou, J. Liu, P. Dai, X. Du, M. Abdel Wahab, Automatic laser profile recognition and fast tracking for structured light measurement using deep learning and template matching, Measurement 169 (2021) 108362, https://doi.org/10.1016/j.measurement.2020.108362.
[45] GB/T 2977-2016, Size designation, dimensions, inflation pressure and load capacity for truck tires. 2016.
[46] GB/T 2978-2014, Size designation, dimensions, inflation pressure and load capacity for passenger car tires. 2014.
[47] Z. Chen, Z.P. Xie, J. Zhang, Measurement of vehicle-bridge-interaction force using dynamic tire pressure monitoring, Mech. Syst. Signal Process. 104 (2018) 370–383, https://doi.org/10.1016/j.ymssp.2017.11.001.
[48] A. Mohsenimanesh, S.M. Ward, M.D. Gilchrist, Stress analysis of a multi-laminated tractor tyre using non-linear 3D finite element analysis, Materials. Design. 30 (4) (2009) 1124–1132, https://doi.org/10.1016/j.matdes.2008.06.040.
[49] JTG E60-2008, Field test procedures for highway subgrade and pavement, Institute of Highway Science, Ministry of Communications. 2008. https://doi.ISBN 978-7-114-07296-3.
[50] D. Liu, Y. Wu, Y. Xu, J. Li, Stochastic response of bistable vibration energy harvesting system subject to filtered Gaussian white noise, Mech. Syst. Signal Process. 130 (2019) 201–212, https://doi.org/10.1016/j.ymssp.2019.05.004.
[51] Q. Liu, A. Shalaby, Simulation of pavement response to tire pressure and shape of contact area, Can. J. Civil. Eng. 40 (3) (2013) 236–242, https://doi.org/10.1139/cjce-2011-0567.
[52] W. Alkasawneh, E. Pan, R. Green, The effect of loading configuration and footprint geometry on flexible pavement response based on linear elastic theory, Road. Materials. Pavement. Design. 9 (2) (2008) 159–179, https://doi.org/10.1080/14680629.2008.9690112.
[53] P.S. Pillai, Y.G. Li, Empirical formula for calculating tire imprint area, Rubber. translation. 2 (1988) 34-37, https://doi.CNKI:SUN:SJXG.0.1988-02-007.
[54] M. Peng, C.F. Gong, Radial stiffness of automobile tire, Tianjin, Automobile 3 (1994) 16–19. https://doi.CNKI:SUN:SXQC.0.1994-04-004.
[55] R.B. Machemehl, F. Wang, J.A. Prozzi, Analytical study of effects of truck tire pressure on pavements with measured tire-pavement contact stress data, Transp. Res. Rec. 1919 (1) (2005) 111–120, https://doi.org/10.1177/0361198105191900112.
[56] D. Jeong, S.B. Choi, J. Lee, M. Kim, H. Lee, Tire dimensionless numbers for analysis of tire characteristics and intelligent tire signals, Mech. Syst. Signal Process. 161 (2021) 107927, https://doi.org/10.1016/j.ymssp.2021.107927.
[57] J.D. Zhuang, Automobile tire, Beijing Institute of Technology Press, 1996 https://doi.ISBN 7-81045-067-0.
[58] L.G. Loría, J.P. Aguiar, A. Vargas, in: The roles of accelerated pavement testing in pavement sustainability engineering, environment, and economics, Springer, 2016, https://doi.org/10.1007/978-3-319-42797-3.